

Supporting Information

Composition-tuned surface binding on CuZn-Ni catalysts boosts CO₂RR selectivity towards CO generation

Jinxi Chen,^{a,#} Xiaofei Wei,^{b,#} Rongming Cai,^a Jiazheng Ren,^a Min Ju,^a Xiaoqing Lu,^b Xia Long,^{a,*} and Shihe Yang^{a,*}

^a Guangdong Provincial Key Lab of Nano-Micro Material Research, School of Chemical Biology and Biotechnology, Shenzhen Graduate School, Peking University, Shenzhen 518055 (China)

^b School of Materials Science and Engineering, China University of Petroleum, Qingdao, Shandong, 266580, PR China

These authors contributed equally to this work

* E-mail: xialong@pku.edu.cn, chsyang@pku.edu.cn

Chemicals

Cupric chloride dihydrate (CuCl₂·2H₂O) (99%), Zinc chloride (ZnCl₂) (99%), Nickel (II) chloride hexahydrate (NiCl₂·6H₂O) (98%), potassium hydroxide (KOH), absolute ethanol (C₂H₅OH) were purchased commercially from Sinopharm Chemical Reagent Co., Ltd. Sodium borohydride (NaBH₄) (98%) was purchased from Aladdin industrial corporation Shanghai China. De-ionized water was used throughout for preparing aqueous solution. All chemicals and reagents were used without further purification.

Synthesis

The typical copper–zinc gels were prepared via reported slightly modified in-situ spontaneous gelation process. To prepare the Cu₁Zn₉ gel, 15 mL of 0.1 M freshly prepared NaBH₄ aqueous solution was added into the mixture of 4.5 mL of 0.1 M ZnCl₂ solution, 0.5 mL of 0.1 M CuCl₂ solution and 5 mL of DI water. The color of the solution turned to black immediately. The resulting solution was rotated at 300 rpm for 1 minute and then kept overnight at room temperature. The gel was formed at the bottom of the beaker. The ratio of Cu to Zn in the gels was controlled by strictly tuning the molar ratio of CuCl₂ and ZnCl₂. Then, the obtained gel was washed with DI water to remove the impurities. Prior to the drying procedure, the supernatant of the gel was carefully exchanged with absolute ethanol. Consequently, the resulting anhydrous ethanol containing gels

were taken into a vacuum drying oven (Model: DZF-6050) at 60 °C for 12 hours. The monometallic Cu and Zn gels with special nanostructures were prepared following the same procedure except in the absence of either of the metal precursor's counterpart. To prepare the Cu₁Zn₉Ni₁ gel, 50 μL of 0.1 M NiCl₂ was immediately added into the reaction solution after adding NaBH₄ aqueous solution.

Material Characterization

Scanning electron microscope (SEM) measurements were carried out on a field emission SEM (ZEISS SUPRA®55). X-ray diffraction data was collected on a diffractometer (D8 Advance, Bruker) with Cu K α radiation (2 θ ranging from 20° to 80°, λ = 1.541 Å, step size = 0.02°). X-ray photoelectron spectroscopy (XPS) studies were carried out on ESCALAB 250Xi (Thermo Fisher). Spectra were analyzed using XPSPEAK software, and the C1s peak for adventitious hydrocarbons at 284.8 eV was used for binding energy calibration. Transmission electron microscopy (TEM) images, high resolution TEM images and electron diffraction patterns were measured with a JEOL JEM-3200FS. The suspensions with catalyst were dropped onto the molybdenum grid for TEM, ED pattern and HRTEM characterization. Atomic force microscopy (AFM, Multimode Nanoscope IIIa, Veeco Instruments) was used to determine the morphology and size of the nanomaterials. UV-visible (UV-vis) absorption spectra were measured on a UV-vis spectrometer (UV-1800, Shimadzu). Raman measurements were performed on a laser Raman spectrometer (HORIBA LabRAM HR800) with a laser excitation wavelength of 532 nm (diode). Electron paramagnetic resonance (EPR) (Magnettech ESR5000, Bruker) was performed to compare the oxygen vacancy concentration in materials.

Electrochemical Measurements

Electrochemical measurements were carried out in a flow-cell three-electrode system at 25 °C on a CHI 760 electrochemistry workstation. A commercial IrO₂ flake was used as the counter electrode and an Hg/HgO electrode was used as reference electrode. The preparation of the working electrode was as follows: 3 mg of catalyst and 2 μL of Nafion (2.5 wt%) was dispersed in 600 μL of ethanol before sonication for 30 min for forming the catalyst ink. 200 μL of the ink was dropped onto a clean carbon paper (3 cm*1 cm) and dried under ambient temperature serving as the working electrode. The potentials were calibrated against the RHE according to the following equation: ($E_{\text{RHE}} = E_{\text{exp.}} + 0.0592 \cdot \text{pH} + E_{\text{Hg/HgO}}$), where $E_{\text{Hg/HgO}}$ is the potential difference measured between the Hg/HgO

electrode and the working electrode, the pH value of the electrolyte solution (1M KOH) was ~13.7, and E_{RHE} is the calibrated potential. Before and during the measurements, the cell was purged continuously with Ar or CO₂ to ensure its gas saturation. The anion exchange membrane, reference electrode and counter electrode were positioned and clamped together between silicone gaskets and flow fields. Then 30 mL of electrolyte (1.0 M KOH aqueous solution) was introduced into the anode chamber between anode and membrane, as well as the cathode chamber between membrane and cathode, respectively. The electrolytes in cathode and anode were circulated by two pumps at the rate of 5 mL min⁻¹. CO₂ gas was continuously supplied to the gas chamber located at the back side of cathode with the rate of 20 sccm. Gas could diffuse into the interface between cathode and electrolyte, thus generating a triple phase interface between gas, electrode, and electrolyte.

The cyclic voltammetry (CV) measurements were performed at a scan rate of 50 mV/s for 30 times until a stable CV curve was achieved before other electrochemical measurements. The polarization curves were obtained using linear sweep voltammetry (LSV) with a scan rate of 10 mV/s sweeping from -0.9 V to -2.0 V (vs. Hg/HgO). All the above electrochemical experiments were carried out without compensating iR drop.

Product Analysis

The reduction reaction was performed by chronoamperometry at different applied potentials. During the chronoamperometry electrolysis, CO₂ was bubbled into the cathodic compartment continuously and vented directly into the gas-sampling loop of a gas chromatograph (Shimadzu GC 2014), which could make the gas phase products periodic quantification.

The FE of CO₂RR is calculated as follows:

$$FE\% = \frac{n_e * \text{flow rate} * nF}{j_{\text{total}}} * 100\%$$

Where n_e is the number of electrons transferred from CO₂ to a given product, n is the number of moles of the target product, and the Faraday constant F is 96485 C mol⁻¹. Partial current density can be calculated in a similar way:

$$j_x = \frac{j_{\text{total}} * FE\%}{\text{geometric surface area}}$$

The n_e of gas products are calculated by using GC detected concentration (ppm):

$$n_e = \frac{P_0 * \frac{Peak\ area}{a}}{RT}$$

Where P_0 is the pressure, T is the temperature, a is the scale factor of the product determined by GC.

Computational Details

All calculations were performed by density functional theory (DFT) with the Vienna Ab initio Simulation Package (VASP) 6.1.1 (Phys. Rev. B. 54 (1996) 11169–11186). The electron-ion interactions were represented by the projector-augmented-wave (PAW) potentials. The Perdew-Burke-Ernzerhof (PBE) exchange-correlation functional within a generalized gradient approximation (GGA) was used in this study (Phys. Rev. Lett, 77 (1996) 3865–3868). The k-points were set to be $2 \times 3 \times 1$ for geometry optimization and 400 eV plane wave energy cutoff was doped for all the computations. The electronic energy and forces were converged to within 1.0×10^{-6} eV and 0.02 eV/Å, respectively. A dispersion correction by DFT-D3 method with the standard parameters were employed to describe the van-der-Waals (VDW) interactions between the reaction intermediates and the catalysts (J. Chem. Phys. 132 (2010) 154104). Solvation effect was considered by employing the VASPsol code (J. Chem. Phys. 140 (2014) 084106). A 15 Å vacuum layer was employed to prevent artificial interactions between periodic images.

The related adsorption energy (E_{ads}) of key reaction intermediates on catalysts were calculated by using the following formula:

$$E_{ads} = E_{M/C} - E_C - E_M$$

where $E_{M/C}$, E_C , and E_M represented the total energy of adsorbed molecule and catalyst, the energy of catalyst, and the energy of adsorbates, respectively. A more negative E_{ads} value represented a more stable adsorption configuration.

The free energy changes (ΔG) of each elementary reaction step during CO₂RR were calculated using the computational hydrogen electrode (CHE) model. In this model, the chemical potential of the (H⁺ + e⁻) is equal to the energy of half of the gas-phase H₂ at 0 V vs reversible hydrogen electrode (RHE) (The Journal of Physical Chemistry B, 2004, 108(46): 17886-17892). The Gibbs free energy was

calculated by the following equation: $G = E + \text{ZPE} + \int C_p dT - TS$. Where zero point energies (ZPE), enthalpic temperature correction ($\int C_p dT$) and entropy correction (TS) were calculated based on vibration analysis at 298.15 K. E denotes the electronic energies calculated by DFT.

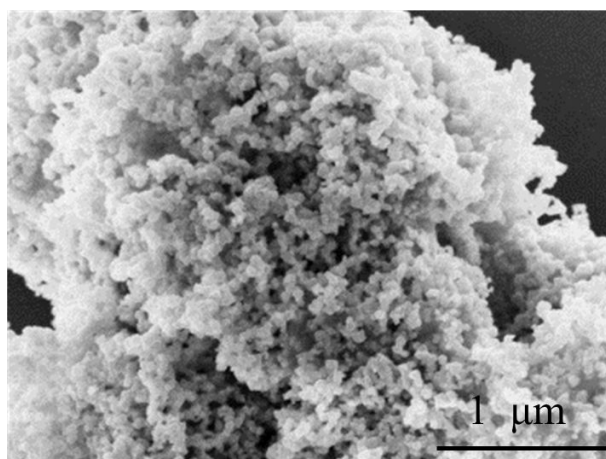


Figure S1. SEM image of Cu aerogel showing typical nanosponge microstructure.

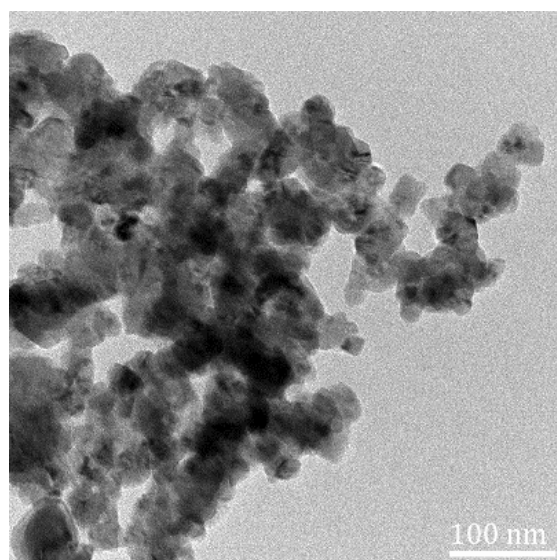


Figure S2. TEM image of Cu aerogel showing typical nanosponge microstructure with nanoparticles as the building blocks.

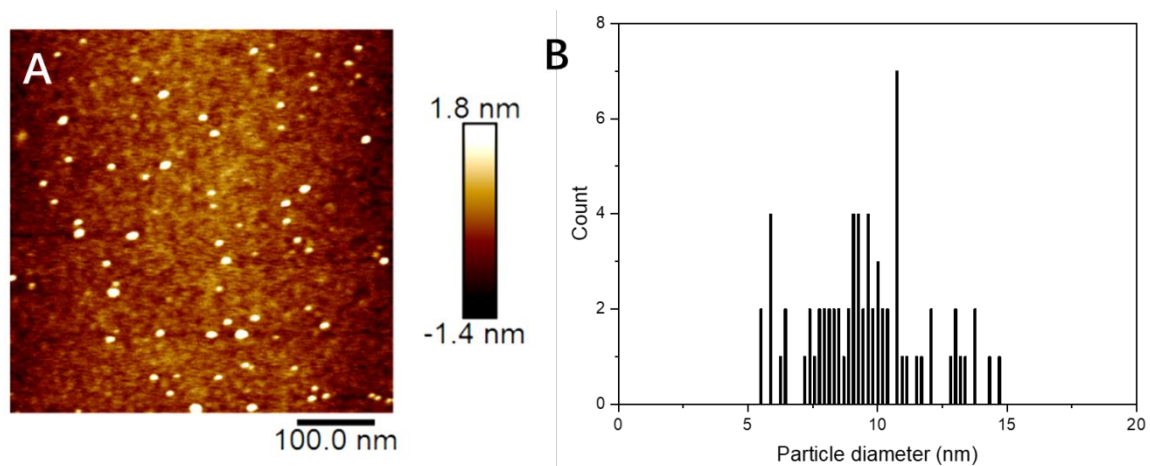


Figure S3. (A) AFM images of Cu aerogel and (B) the corresponding size distribution of the nanoparticles in (A).

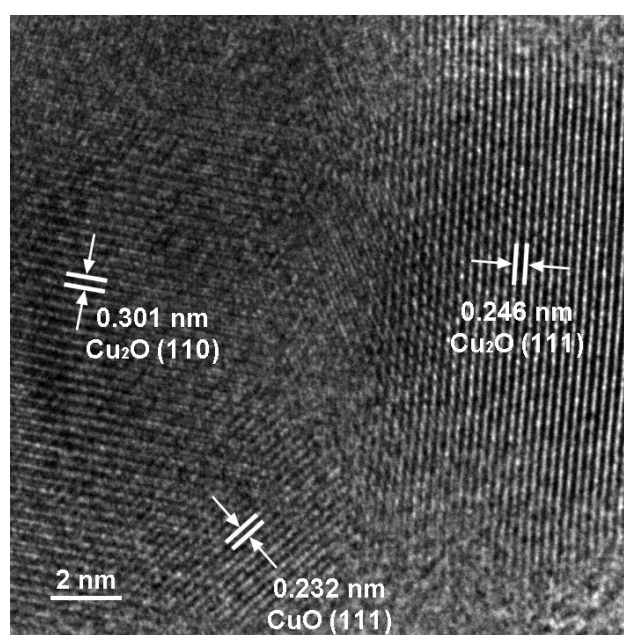


Figure S4. HRTEM images of Cu aerogel.

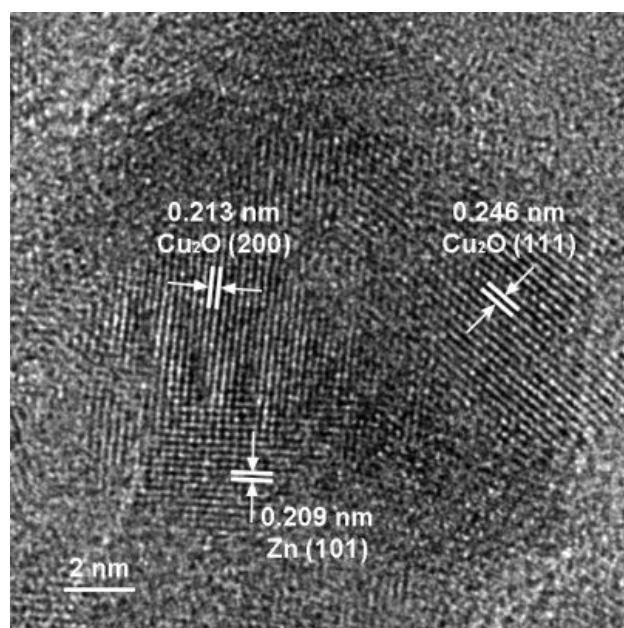


Figure S5. HRTEM images of Cu₉Zn₁₁.

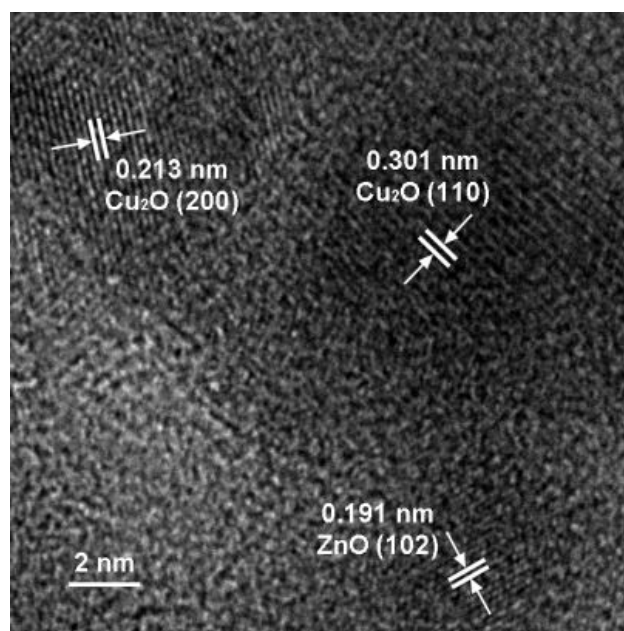


Figure S6. HRTEM images of Cu₅Zn₅.

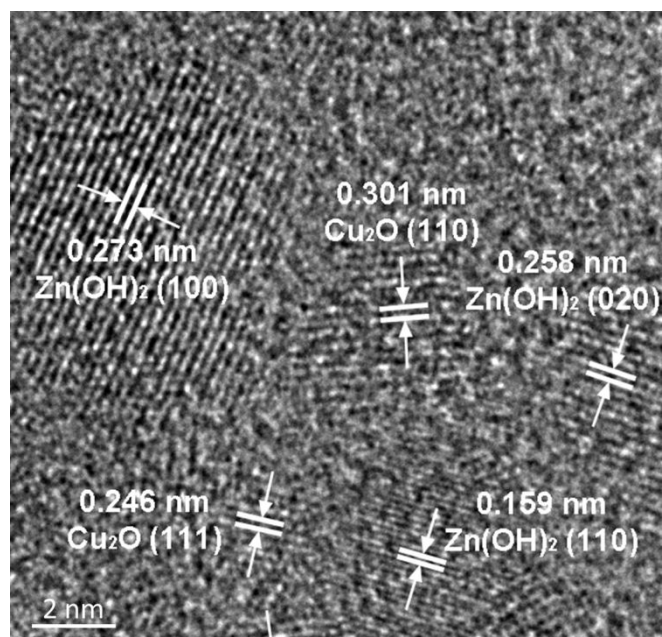


Figure S7. HRTEM images of Cu_1Zn_9 .

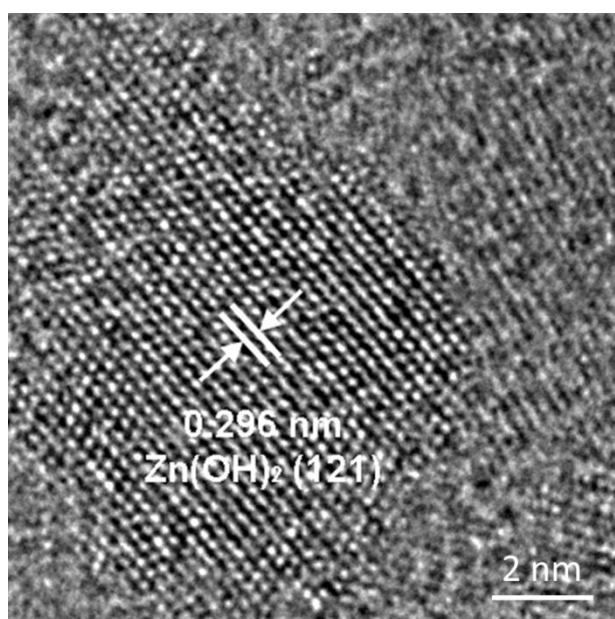


Figure S8. HRTEM images of Zn aerogel.

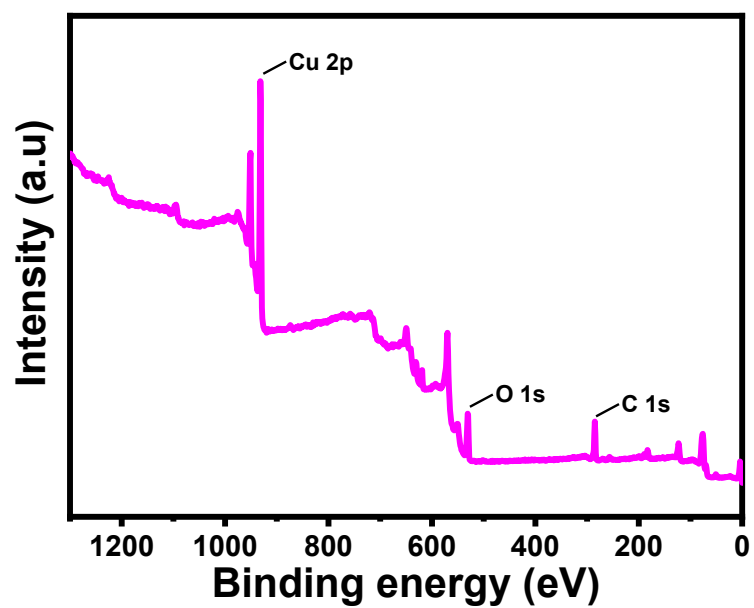


Figure S9. Full XPS spectrum of Cu aerogel.

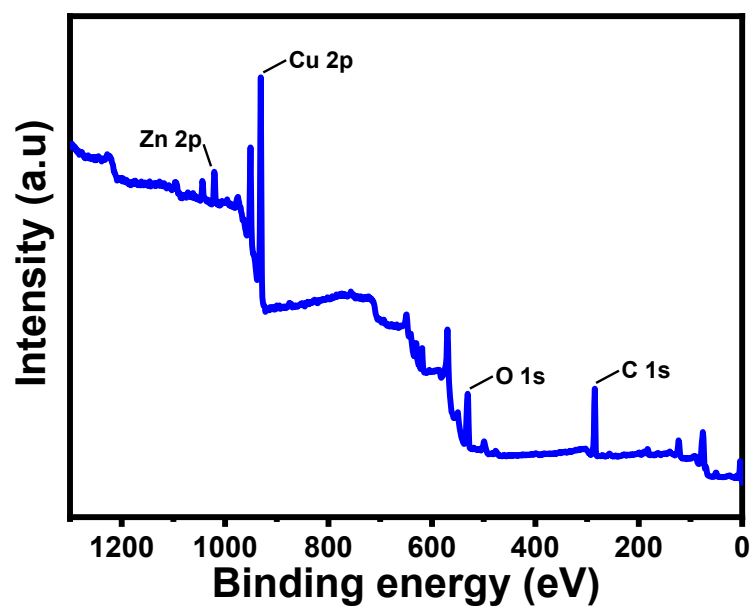


Figure S10. Full XPS spectrum of Cu₉Zn₁.

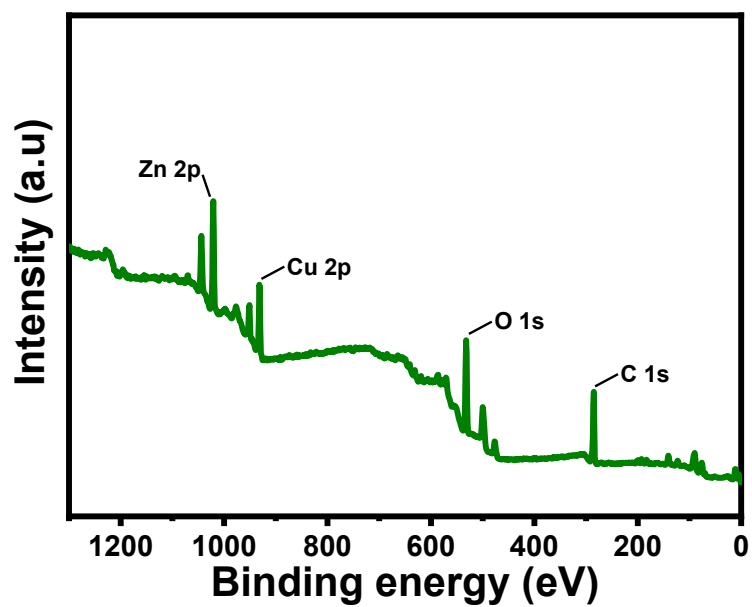


Figure S11. Full XPS spectrum of Cu_5Zn_5 .

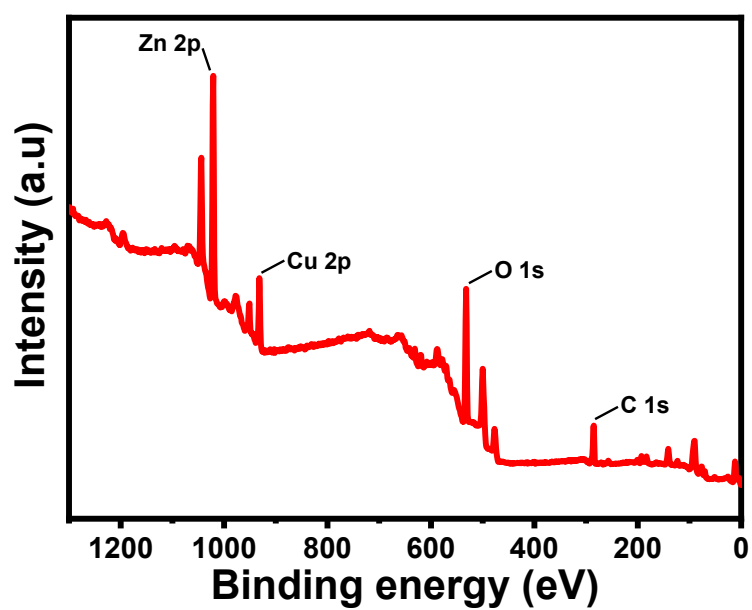


Figure S12. Full XPS spectrum of Cu_1Zn_9 .

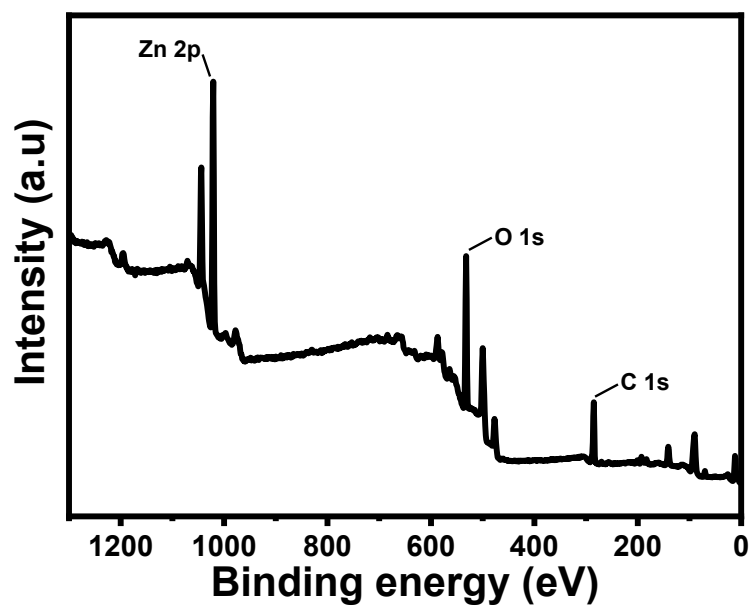


Figure S13. Full XPS spectrum of Zn aerogel.

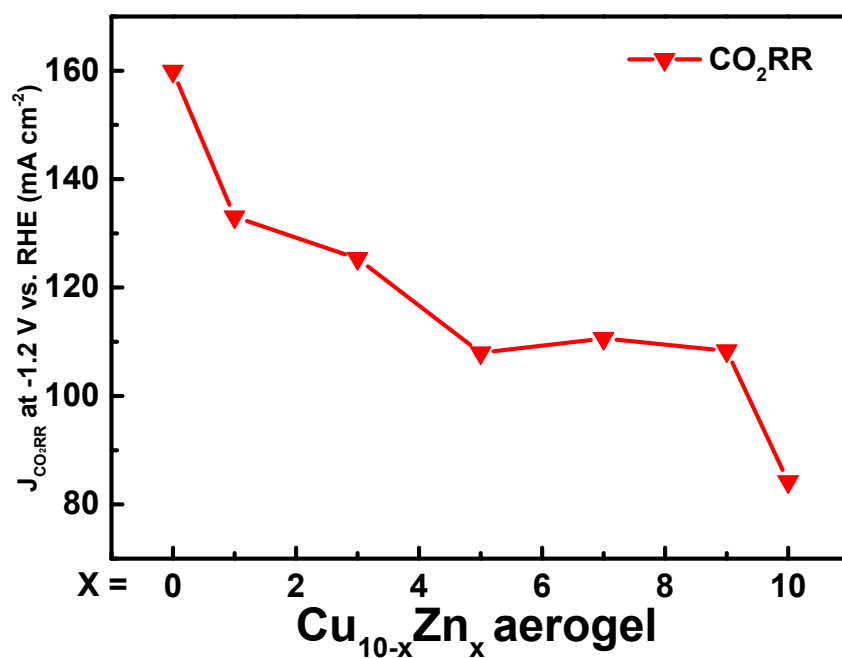


Figure S14. The partial current density of CO₂RR measured at E= -1.2 V vs RHE as the function of Zn concentration in Cu_{10-x}Zn_x aerogel.

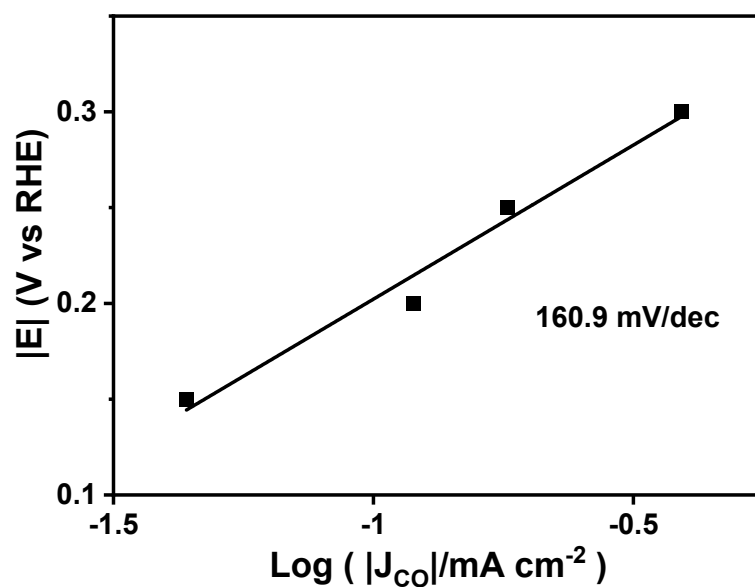


Figure S15. Tafel plot of CO₂RR on Cu aerogel.

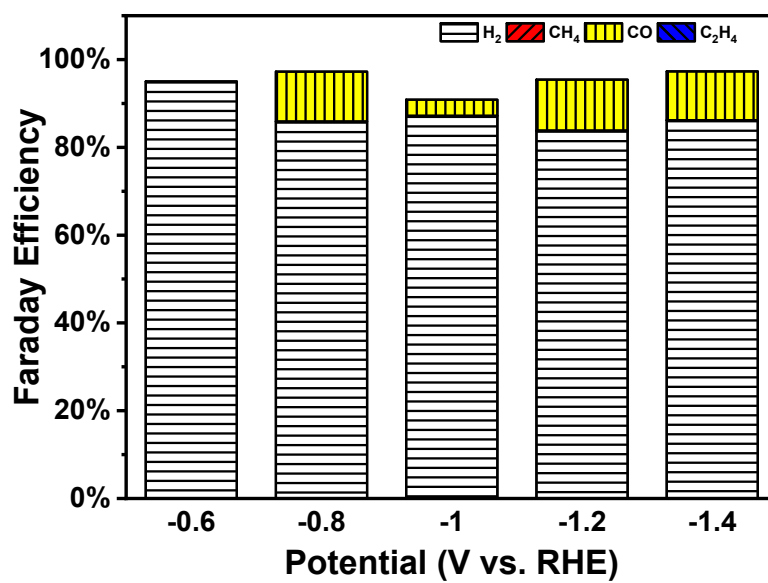


Figure S16. FE of all gas products tested on bare carbon electrode for alkali CO₂RR in flow cell.

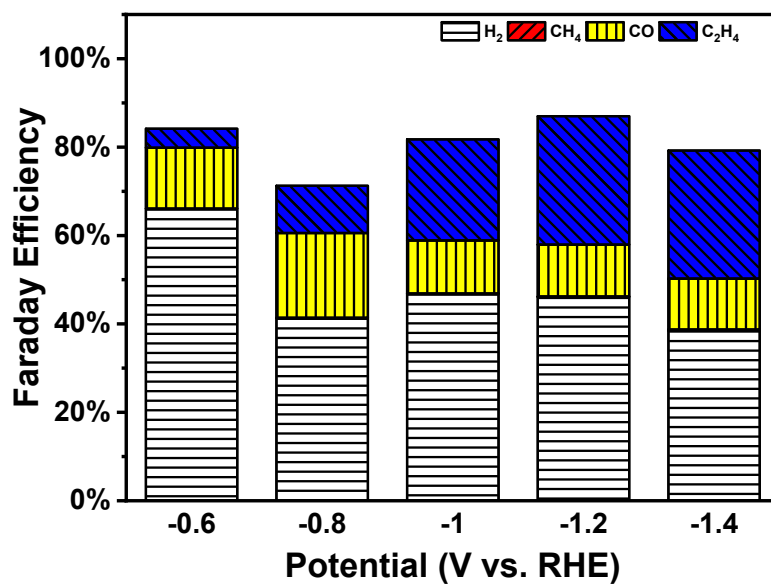


Figure S17. FE of all gas products tested on metallic Cu electrode for alkali CO₂RR in flow cell.

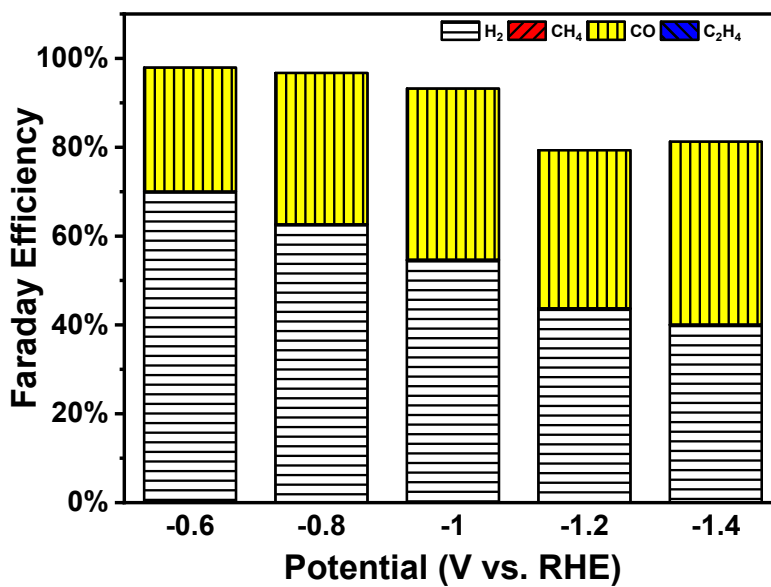


Figure S18. FE of all gas products tested on metallic Zn electrode for alkali CO₂RR in flow cell.

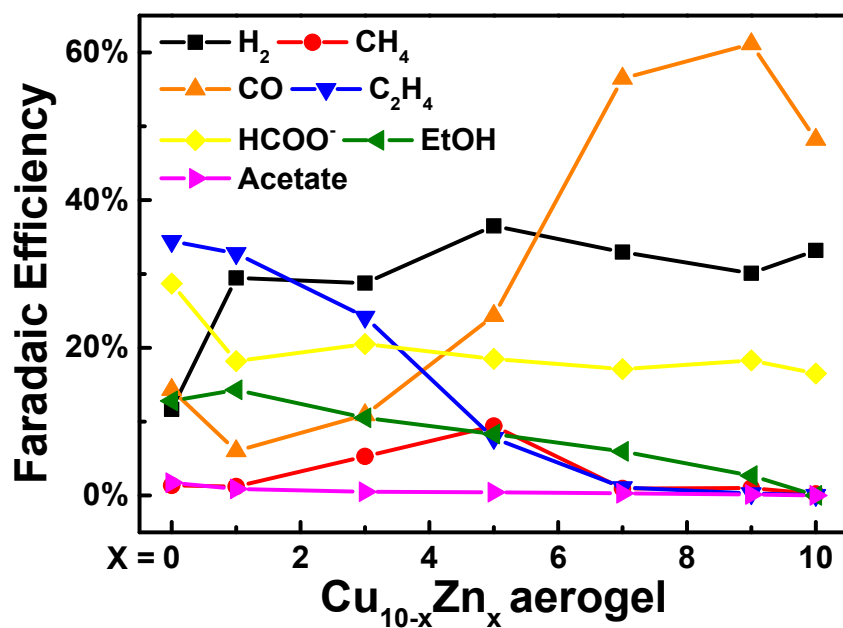


Figure S19. The Faradaic efficiency of CO₂RR products measured at E= -1.2 V vs RHE as the function of Zn concentration in Cu_{10-x}Zn_x aerogel.

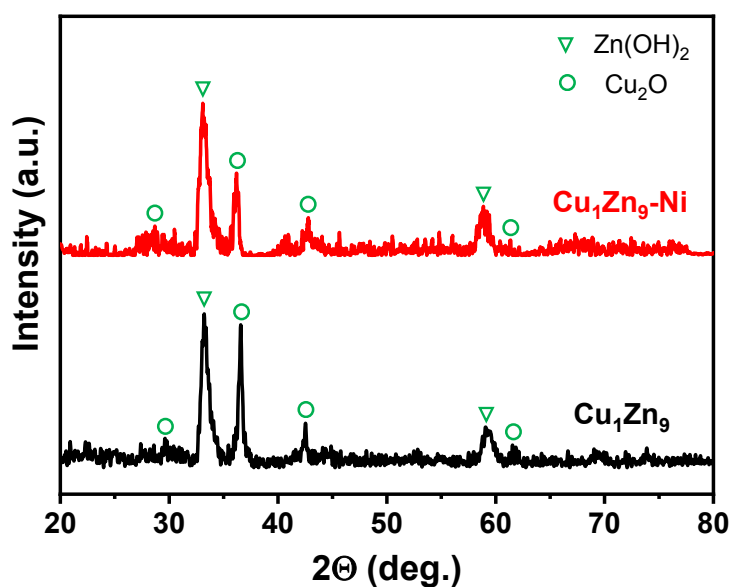


Figure S20. XRD spectra of Cu₁Zn₉ and Cu₁Zn₉-Ni.

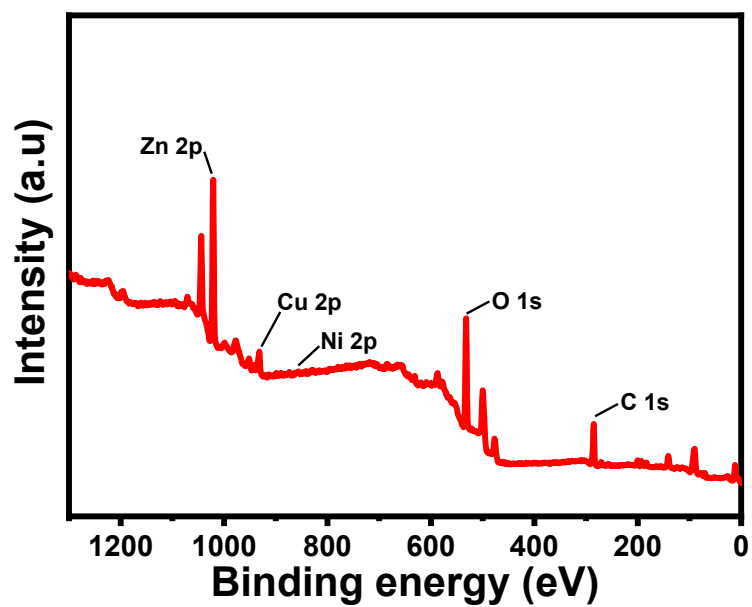


Figure S21. Full XPS spectrum of $\text{Cu}_1\text{Zn}_9\text{-Ni}$.

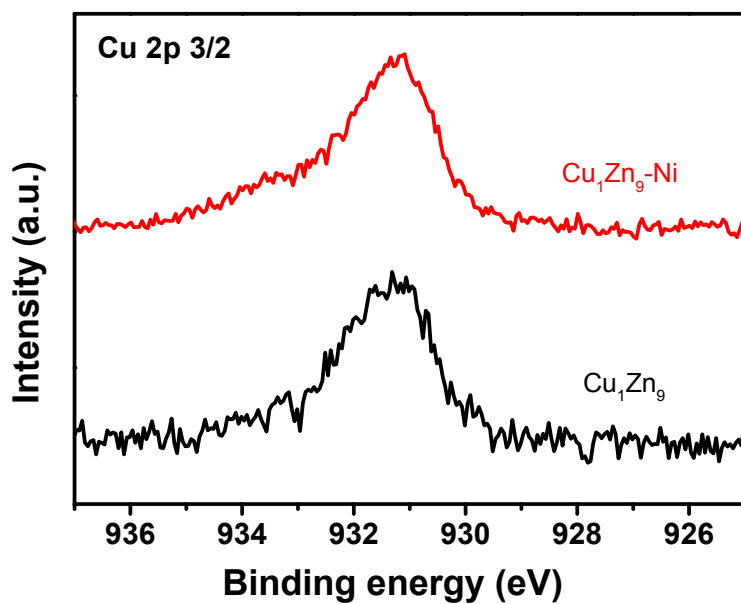


Figure S22. High resolution XPS spectra of Cu_1Zn_9 and $\text{Cu}_1\text{Zn}_9\text{-Ni}$ at Cu 2p spin-orbital.

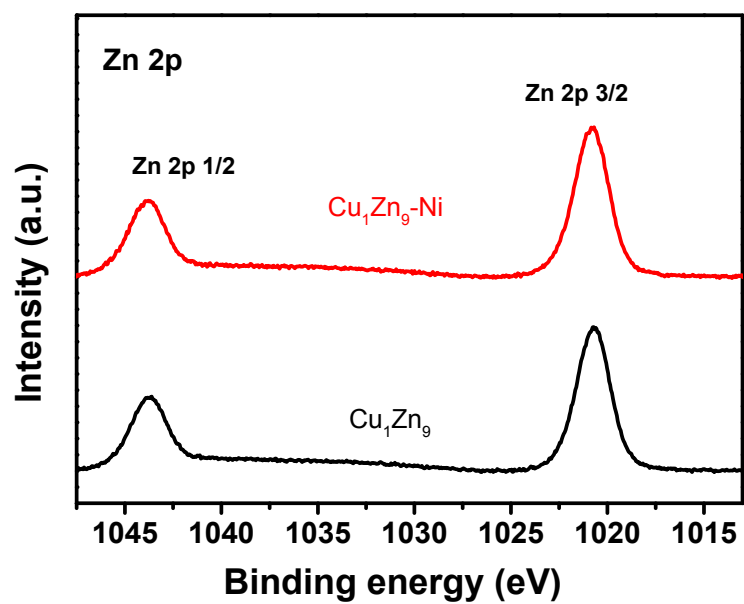


Figure S23. High resolution XPS spectra of Cu_1Zn_9 and $\text{Cu}_1\text{Zn}_9\text{-Ni}$ at Zn 2p spin-orbital.

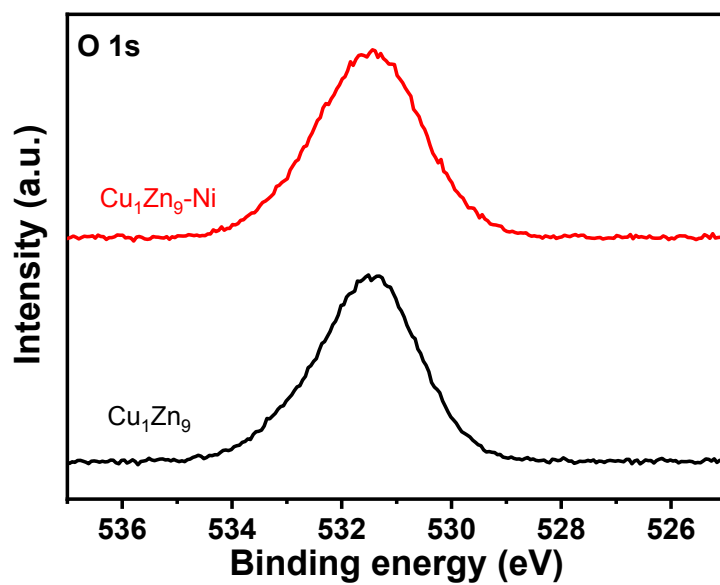


Figure S24. High resolution XPS spectra of Cu_1Zn_9 and $\text{Cu}_1\text{Zn}_9\text{-Ni}$ at O 1s spin-orbital.

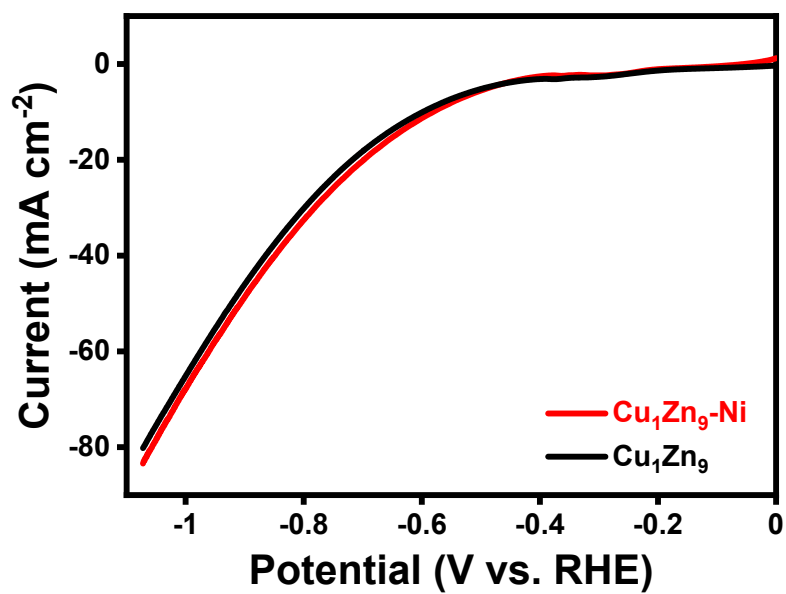


Figure S25. LSV comparison of Cu_1Zn_9 and $\text{Cu}_1\text{Zn}_9\text{-Ni}$.

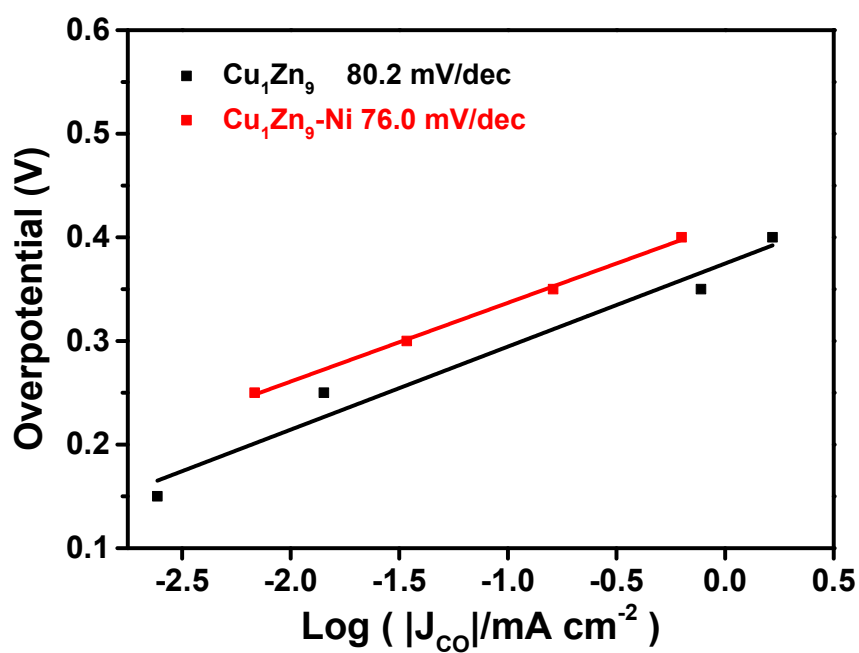


Figure S26. Tafel slope comparison of Cu_1Zn_9 and $\text{Cu}_1\text{Zn}_9\text{-Ni}$.

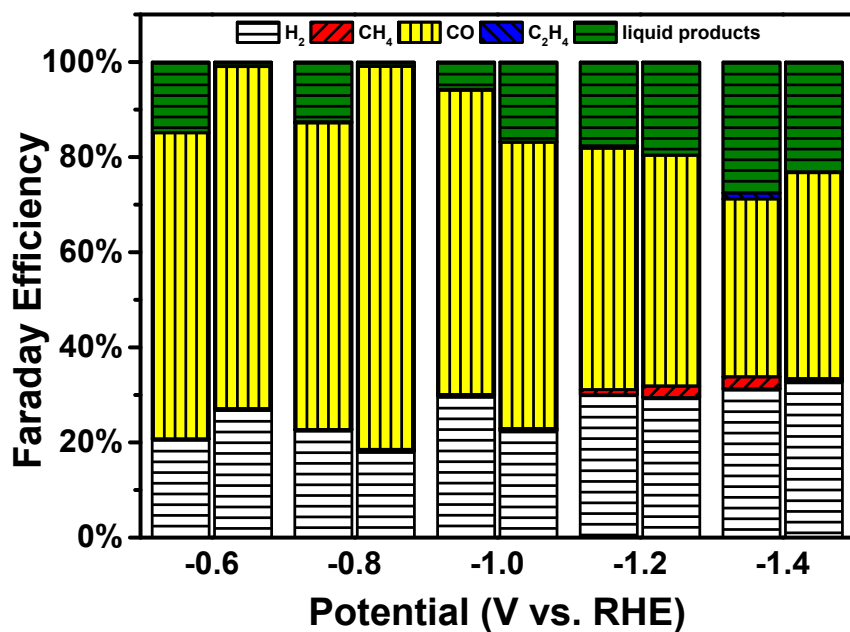


Figure S27. FE of all products collected on Cu₁Zn₉-Ni for alkali CO₂RR in flow cell. Left column: Cu₁Zn₉, right column: Cu₁Zn₉-Ni.

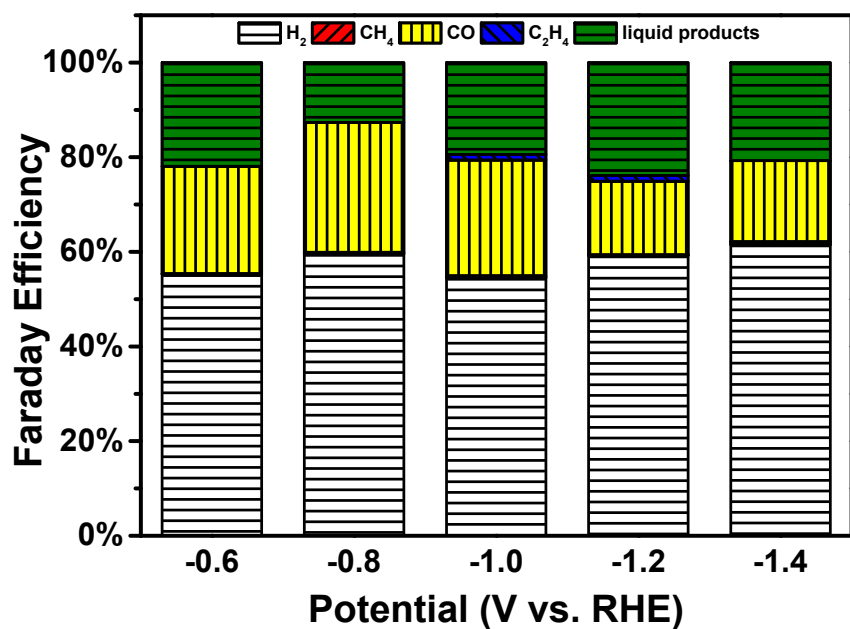


Figure S28. FE of all products collected on Cu₁Zn₉-Ni with increased Ni concentration (increased from 1% to 5%) for alkali CO₂RR in flow cell.

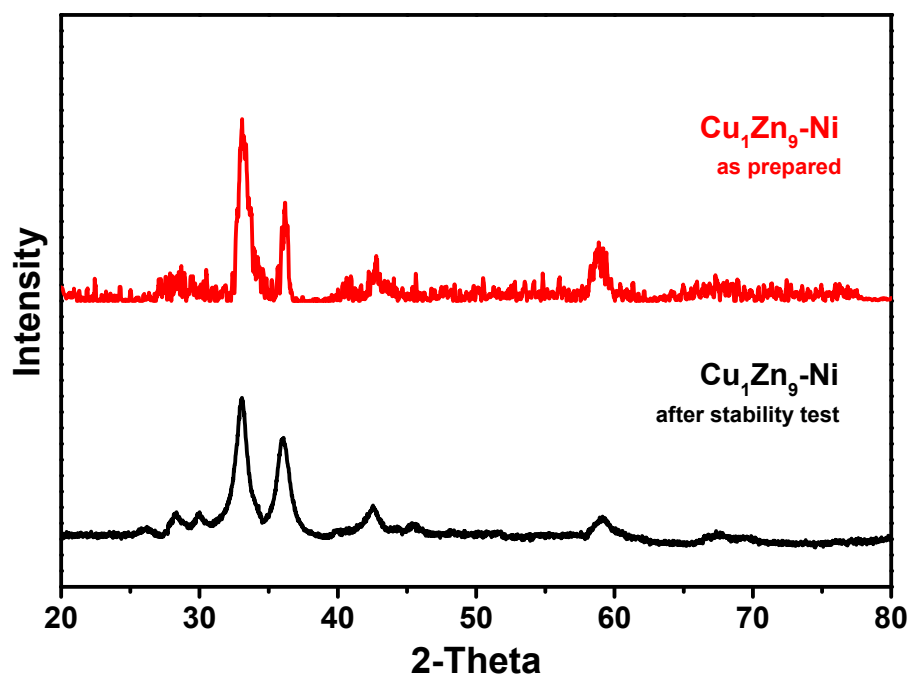


Figure S29. XRD patterns of the prepared Cu₁Zn₉-Ni before and after electrochemical stability tests.

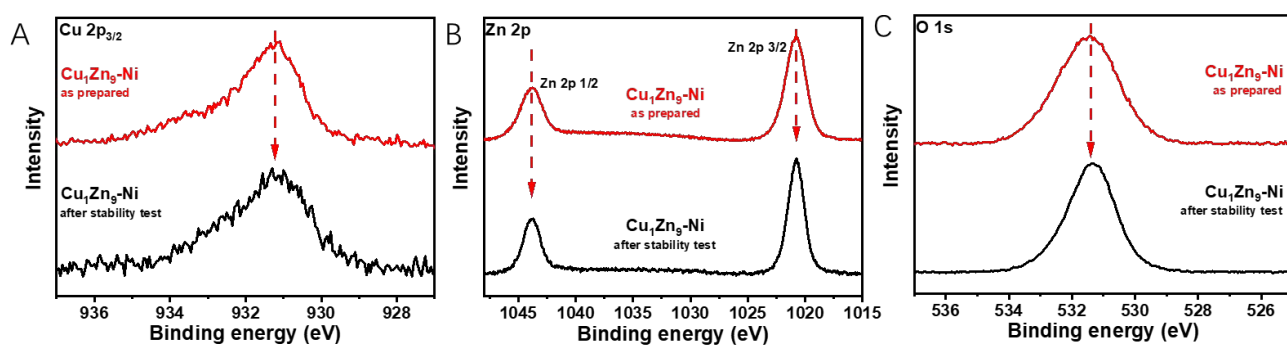


Figure S30. High resolution XPS spectra at (A) Cu 2p, (B) Zn 2p, and (C) O 1s, of the prepared Cu₁Zn₉-Ni before and after electrochemical stability tests.

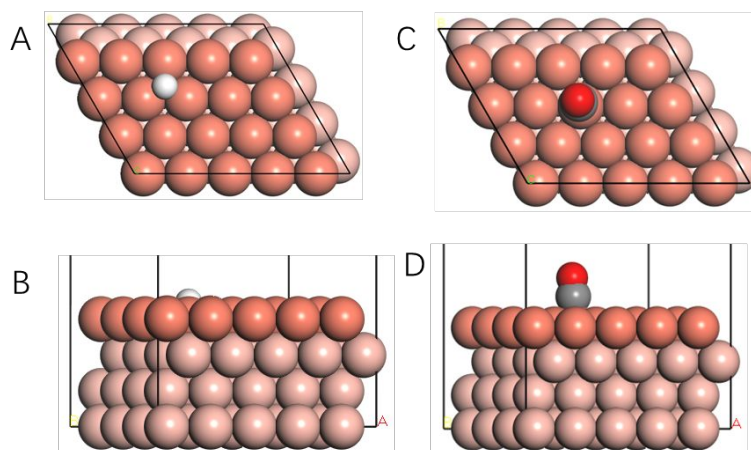


Figure S31. (A, C) top view and (B, D) side view images of adsorption of (A,B) H^* and (C, D) CO^* on Cu (111) surface.

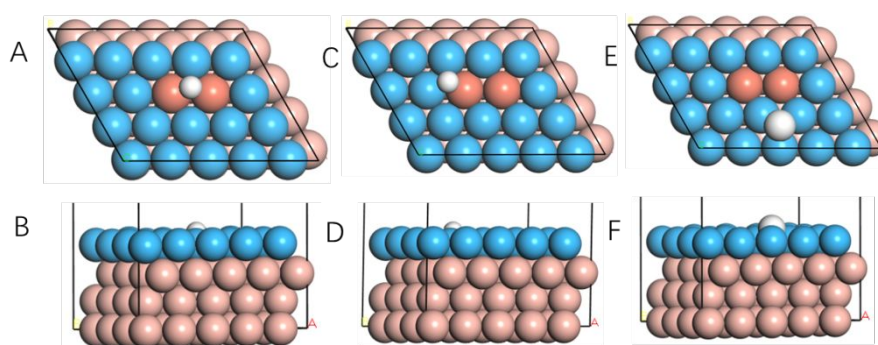


Figure S32. (A, C, E) top view and (B, D, F) side view images of adsorption of H^* on the Cu and the surrounding two Zn atoms of Cu_1Zn_9 aerogel.

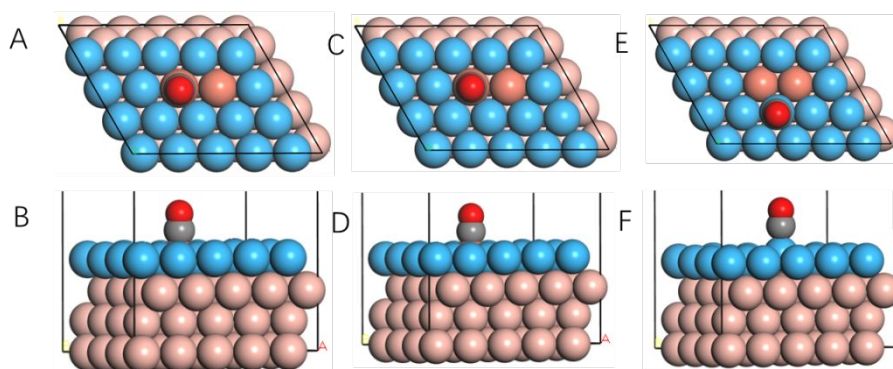


Figure S33. (A, C, E) top view and (B, D, F) side view images of adsorption of CO^* on the Cu and the surrounding two Zn atoms of Cu_1Zn_9 aerogel.

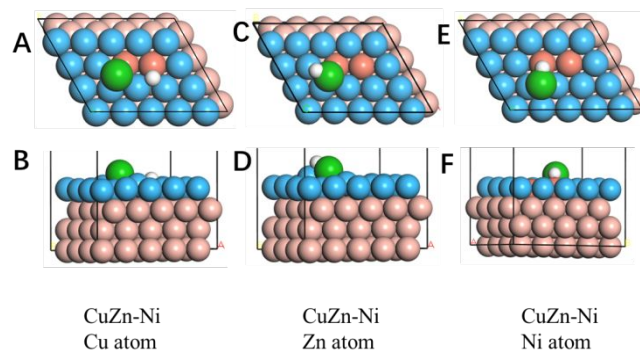


Figure S34. (A, C, E) top view and (B, D, F) side view images of adsorption of $^*\text{H}$ on the Cu, Zn and Ni atoms of $\text{Cu}_1\text{Zn}_9\text{-Ni}$ aerogel.

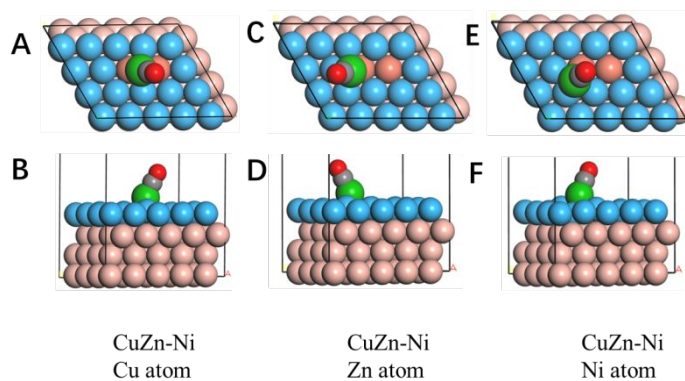


Figure S35. (A, C, E) top view and (B, D, F) side view images of adsorption of $^*\text{CO}$ on the Cu, Zn and Ni atoms of $\text{Cu}_1\text{Zn}_9\text{-Ni}$ aerogel.

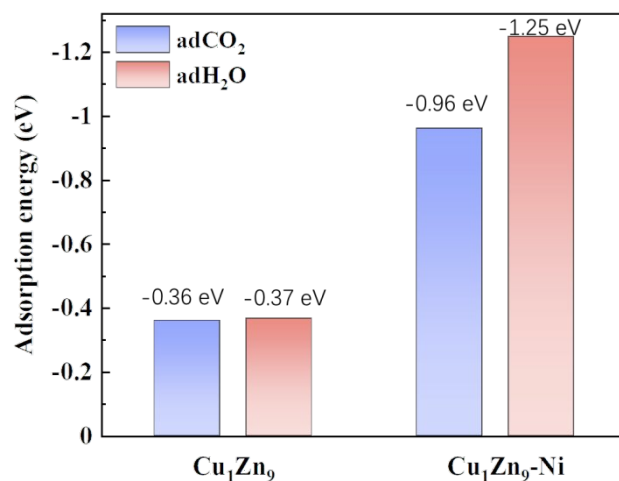


Figure S36. Adsorption energy (E_{ad}) of CO₂ and H₂O on the surface of Cu₁Zn₉ and Cu₁Zn₉-Ni.

Table S1. Atomic concentration of Cu, Zn and Ni in the as-prepared alloy aerogels calculated from XPS spectra.

Samples	Zn	Cu ₁ Zn ₉	Cu ₃ Zn ₇	Cu ₅ Zn ₅	Cu ₇ Zn ₃	Cu ₉ Zn ₁	Cu	Cu ₁ Zn ₉ -Ni
Cu (%)		1.5	4.22	3.64	5.65	15.7	24.55	1.75
Zn (%)	14.39	13.33	11.26	4.86	2.43	1.74		15.77
Ni (%)								0.18